

Ultrashort Space- and Time-Scales: Need for a Quantum Description

In Sect. 1.3 we have introduced the basic concepts of the semiclassical picture. In that formulation several assumptions were more or less explicitly made that require some considerations. As we shall see, the latter are not always justified in new-generation semiconductor nanomaterials and nanodevices, so that fully quantum-mechanical treatments of the problem are imperative.

2.1 Intrinsic Limitations of the Semiclassical Picture

In order to decide if the semiclassical treatment is good enough, it is crucial to decide how good is good enough. To this aim, an acceptable energy uncertainty $\delta\epsilon$ is to be established. Its definition is somewhat arbitrary and it depends upon the particular phenomenon under investigation: It may coincide with a characteristic system quantity, e.g., the thermal energy, or may correspond to the energy resolution of our experimental apparatus.

In order to proceed with our analysis, a few characteristic quantities should be introduced. Their definitions are, for the moment, not rigorous; only their intuitive meaning is needed for the purpose of the present discussion. They are the mean scattering time τ_s (between two successive scattering processes), the corresponding electronic mean free path ℓ , and the collision duration τ_c ; furthermore, in ultrafast electro-optical processes two other experimental times are relevant: the observation time, i.e., the time elapsed from the preparation of the initial condition to the time of the optical measurement, and the time resolution of the experimental apparatus.

Let us now reconsider the most relevant assumptions made in the semiclassical treatment.

- (i) During the so-called free flight (between two successive scattering processes) electrons are treated as classical particles with well-defined positions and momenta. For this approximation to be acceptable, one must be able to conceive electronic wavepackets with a momentum uncertainty

much smaller than their average momentum ($\Delta p \ll p$) and, at the same time, with a position uncertainty much smaller than the electronic mean free path ($\Delta r \ll \ell$); taking into account that $\ell \sim \frac{p}{m^*} \tau_s$, from the uncertainty relation we have

$$\hbar \sim \Delta r \Delta p \ll \ell p \sim \frac{p^2}{m^*} \tau_s . \quad (2.1)$$

Since the energy value $\frac{p^2}{m^*}$ is always defined within our energy uncertainty $\delta\epsilon$, in order to fulfill the condition in (2.1) for any value of the electron momentum p , it is necessary to ask that:

$$\tau_s \gg \frac{\hbar}{\delta\epsilon} . \quad (2.2)$$

We are then forced to conclude that such semiclassical scenario becomes questionable for values of the mean scattering time τ_s comparable or smaller than the characteristic time $\frac{\hbar}{\delta\epsilon}$; as we shall see, this is equivalent to state that the mean scattering time τ_s should be much larger than the so-called collision duration.

- (ii) In the traditional semiclassical picture, collisions are assumed to be point-like and instantaneous. Since the interaction process between the electron and a given scattering agent has always a finite duration, this last assumption is not correct in general, not even within a purely classical framework; however, in the usual weak-coupling limit, when scattering events are sufficiently rare, the collision duration τ_c may be safely neglected (with respect to the mean scattering time τ_s) and the assumption of instantaneous scattering processes is reasonable. In contrast, in the presence of a strong scattering dynamics, the collision duration τ_c becomes comparable with the mean scattering time τ_s , and for such regimes a detailed analysis of the collision duration is imperative; however, the estimate of τ_c is somewhat arbitrary because the concept of collision duration itself is ill-defined. In very general terms, from basic perturbation theory (see, e.g., [86]) we know that the final state of a scattering process is defined within an energy range $\delta\epsilon$ of the order of $\frac{\hbar}{\tau_c}$, where τ_c is the time elapsed after the initial condition/preparation of the scattering process. The collision duration can then be estimated, in general, with reference to the desired precision $\delta\epsilon$ of the electron energy according to

$$\tau_c \sim \frac{\hbar}{\delta\epsilon} . \quad (2.3)$$

As anticipated, the result in (2.2) may also be written as

$$\tau_s \gg \tau_c , \quad (2.4)$$

i.e., the mean scattering time should be much longer than the collision duration. When such a condition is not fulfilled, we deal with the so-called

multiple-scattering phenomenon, i.e., a scattering process starts before the completion of the previous ones; the neglect of such multiple scattering effects is known as “completed-collision limit.”

For the study of quasiequilibrium electron-transport phenomena at room temperature, the energy uncertainty $\delta\epsilon$ is of the order of $k_B T \sim 25 \text{ meV}$, and therefore, we have

$$\tau_c \sim \frac{\hbar}{k_B T} \sim 10^{-14} \text{ s} . \quad (2.5)$$

We stress, however, that in low-temperature optical experiments the energy uncertainty $\delta\epsilon$ may be strongly influenced/limited also by the resolution of our experimental apparatus, and therefore, the corresponding collision duration τ_c may strongly depend on the particular phenomenon under investigation.

- (iii) During the collision time τ_c , the presence of an intense electro-optical excitation may induce a significant drift of both the initial and final electron wavevectors \mathbf{k} and \mathbf{k}' ; however, since the energy dispersion is not a linear function of \mathbf{k} , the energy difference between initial and final states $(\epsilon_{\mathbf{k}'\nu} - \epsilon_{\mathbf{k}\nu})$ varies with time, and the quantum-mechanical interference process that generates the transition may be significantly modified by the presence of the field. Such a process, called “intracollisional field effect” (ICFE) (see, e.g., [87, 88] and references therein), may introduce significant modifications to the standard scattering rates obtained via the conventional second-order perturbation theory within a field-free basis. In order to estimate the relevance of this effect, one may compare the energy imparted to the electron by the external field during the collision, with the average electron energy. A well-established result is that for static fields larger than 10^5 V/cm the ICFE starts to play a significant role. A rigorous microscopic treatment of this phenomenon is given in Sect. 3.4.

To the above discussion we should add that modern technology provides conventional semiconductor devices much smaller than $0.1 \mu\text{m}$ (see, e.g., [89]), characterized by local fields as high as 10^6 V/cm ; furthermore, ultrafast spectroscopy has now reached a time resolution of a few femtoseconds [90–92], i.e., shorter than 10^{-14} s . A few basic conclusions are then in order.

- (a) In conventional semiconductor devices, electric fields are attainable, for which the ICFE has to be taken into account.
- (b) At such fields electrons reach energies of the order of or larger than 1 eV , for which the mean scattering time τ_s between collisions may reach the limiting value of 10^{-14} s , and therefore many of the semiclassical approximations fail.
- (c) The time resolution of modern ultrafast electro-optical technology may be comparable or shorter than the collision duration τ_c itself.

As a general conclusion, it seems clear that a quantum approach to the problem [93–105] – essential for the design and optimization of genuine quantum

devices – is also imperative for the simulation of conventional semiconductor devices, i.e., devices based on classical operation principles.

2.2 Semiclassical Versus Quantum Treatments

In order to clarify the concept of quantum-mechanical phase coherence – and thus the fundamental link between semiclassical and quantum treatments – let us consider the simplest physical model for the description of light–matter interaction, i.e., an optically driven two-level system (see, e.g., [106]). Within a two-level picture, a ground state a with energy ϵ_a and an excited state b with energy ϵ_b are mutually coupled by a driving force, e.g., due to an external electromagnetic field. The total system Hamiltonian written in the noninteracting-level basis $\{|a\rangle, |b\rangle\}$ is given by

$$\hat{H} = \hat{H}_0 + \hat{H}' = \begin{pmatrix} \epsilon_a & 0 \\ 0 & \epsilon_b \end{pmatrix} + \begin{pmatrix} 0 & U_{ab} \\ U_{ba} & 0 \end{pmatrix}. \quad (2.6)$$

This is the sum of a diagonal free-level contribution and of a non-diagonal coupling term; the latter will induce transitions from state $|a\rangle$ to state $|b\rangle$ and vice versa according to the coupling constant $U_{ba} = U_{ab}^*$.

In the absence of interlevel coupling ($U_{ab} = 0$), one deals with two noninteracting stationary states

$$|\psi_a(t)\rangle = e^{-\frac{i\epsilon_a t}{\hbar}} |a\rangle, \quad |\psi_b(t)\rangle = e^{-\frac{i\epsilon_b t}{\hbar}} |b\rangle, \quad (2.7)$$

corresponding to our electron in level a or b , respectively.

In contrast, in the presence of interlevel coupling, the quantum-mechanical state of the system will be given by a linear superposition of the noninteracting states¹:

$$|\psi(t)\rangle = c_a(t)|a\rangle + c_b(t)|b\rangle. \quad (2.8)$$

By inserting the above linear combination into the time-dependent Schrödinger equation

$$i\hbar \frac{d|\psi\rangle}{dt} = \hat{H}|\psi\rangle, \quad (2.9)$$

it is easy to get the following set of Schrödinger-like equations for the two coefficients:

¹ As we shall discuss in Chap. 10, the present quantum-mechanical two-level system is the physical realization of the so-called quantum bit (qubit), i.e., the quantum generalization of the concept of classical-information bit. In this context, the so-called computational state $|\psi\rangle$ is expressed as a generic superposition of the two basis states $|a\rangle$ and $|b\rangle$; the latter are typically referred to as “computational basis,” and are denoted by $|0\rangle$ and $|1\rangle$, respectively.

$$\begin{aligned}
i\hbar \frac{dc_a}{dt} &= \epsilon_a c_a + U_{ab} c_b \\
i\hbar \frac{dc_b}{dt} &= \epsilon_b c_b + U_{ba} c_a .
\end{aligned} \tag{2.10}$$

Again, we see that in the absence of interlevel coupling ($U = 0$) the time variation of the coefficients is simply given by their energy rotations in (2.7), i.e., if the system is prepared in state a or state b it will remain in such eigenstate. In contrast, the presence of the interlevel coupling induces a non-trivial time variation of the two coefficients.

As anticipated, the above two-level model provides the simplest description of light-matter interaction in atomic and molecular systems (see, e.g., [106]) as well as in solids (see, e.g., [90]). Let us now start our analysis by considering two limiting cases: the ultrashort- and continuous-excitation regimes.

An ultrashort optical excitation can be described in terms of a delta-like light pulse: $U_{ab}(t) = \eta \delta(t)$. In this case, the equations of motion (2.10) can be solved analytically: Due to such excitation, the two-level system at time $t = 0$ will undergo an instantaneous transition from its ground state $\{c_a = 1, c_b = 0\}$ to the excited state $\{c_a = \cos \alpha, c_b = -i \sin \alpha\}$, with $\alpha = \frac{\eta}{\hbar}$. Therefore, after the pulse the two-level system will be in the excited state

$$|\psi(t)\rangle = \left(\cos \alpha e^{-\frac{i\epsilon_a t}{\hbar}} \right) |a\rangle + \left(-i \sin \alpha e^{-\frac{i\epsilon_b t}{\hbar}} \right) |b\rangle , \tag{2.11}$$

which is a coherent quantum-mechanical superposition of the two noninteracting states; indeed, in addition to a finite occupation probability $|c_b|^2 = \sin^2 \alpha$ of the excited state, there exists a well-defined phase coherence between the ground- and the excited-state contributions, i.e., apart from their amplitudes, the coefficients c_a and c_b exhibit a time-dependent phase difference given by

$$c_b(t) c_a^*(t) \propto e^{-i\omega_o t} , \tag{2.12}$$

where $\omega_o = \frac{\epsilon_b - \epsilon_a}{\hbar}$ is the interlevel energy splitting in units of \hbar . As discussed in [107], this phenomenon is what is generally meant by optically induced phase coherence.

As second limiting case, let us now consider a continuous optical excitation resonant with our two-level system: $U_{ab}(t) = U_o e^{i\omega_o t}$. Also for this case, the set of equations (2.10) can be solved analytically. In particular, taking again as initial condition the system ground state, in this case we get

$$|\psi(t)\rangle = \left(\cos \left(\frac{1}{2} \omega_R t \right) e^{-\frac{i\epsilon_a t}{\hbar}} \right) |a\rangle + \left(-i \sin \left(\frac{1}{2} \omega_R t \right) e^{-\frac{i\epsilon_b t}{\hbar}} \right) |b\rangle , \tag{2.13}$$

where $\omega_R = \frac{2U_o}{\hbar}$ is the so-called Rabi frequency. Compared to the previous case in (2.11), the continuous excitation gives rise to a periodic population and depopulation of the excited state according to $|c_b|^2 = \sin^2(\frac{1}{2}\omega_R t)$. This purely coherent phenomenon is known as “Rabi-oscillation regime.” Moreover,

exactly as for the previous case, the excited state in (2.13) exhibits again the quantum-mechanical phase relation in (2.12). This clearly shows that the time-dependent quantum state (2.13) is characterized by two distinct time-scales, corresponding to the Rabi frequency ω_R and to the interlevel frequency ω_o : the first one – proportional to the amplitude U_o of the applied field – may be detected by measuring semiclassical quantities only, namely the ground- and excited-state populations $|c_a|^2 = \cos^2(\frac{1}{2}\omega_R t)$ and $|c_b|^2 = \sin^2(\frac{1}{2}\omega_R t)$; the second one, in contrast, does not influence the state populations and can only be detected via phase-sensitive optical experiments (see Sect. 2.5), i.e., measurements able to detect the quantum-mechanical phase coherence in (2.12).

For an electromagnetic excitation of arbitrary temporal shape $U_{ab}(t)$ no analytical solution is available, and the set in (2.10) needs to be solved numerically. More specifically, the intermediate regime – between the ultrafast- and the continuous-excitation ones introduced so far – will correspond to an excitation pulse of finite duration, typically written as

$$U_{ab}(t) = U_p(t)e^{i\omega_p t}, \quad (2.14)$$

where the pulse shape $U_p(t)$ is characterized by a time-scale τ_p . When the latter is much longer than the interlevel time-scale (i.e., $\tau_p\omega_o \gg 1$) and the excitation amplitude is small (i.e., $|U_{ab}(t)| \ll \hbar\omega_o$), the excitation process may be considered adiabatically slow, and the previous fully quantum-mechanical description may be safely replaced by an effective semiclassical description based on the well-known Fermi's golden rule.

To this aim, let us go back to the set of equations (2.10), whose formal solution can always be written as

$$\begin{aligned} c_a(t) &= e^{-\frac{i\epsilon_a t}{\hbar}} c_a(0) + \int_0^t dt' e^{-\frac{i\epsilon_a(t-t')}{\hbar}} \frac{U_{ab}(t')}{i\hbar} c_b(t') \\ c_b(t) &= e^{-\frac{i\epsilon_b t}{\hbar}} c_b(0) + \int_0^t dt' e^{-\frac{i\epsilon_b(t-t')}{\hbar}} \frac{U_{ba}(t')}{i\hbar} c_a(t'). \end{aligned} \quad (2.15)$$

Following a standard perturbation scheme discussed in general terms in Chap. 3, by iteratively substituting this formal solution into itself and by limiting the resulting expansion to first-order contributions in the electromagnetic field U_{ab} , we get

$$\begin{aligned} c_a(t) &= e^{-\frac{i\epsilon_a t}{\hbar}} c_a(0) + \frac{2\pi U_{ab}(t) D(\omega_o - \omega_p)}{i\hbar} c_b(t) \\ c_b(t) &= e^{-\frac{i\epsilon_b t}{\hbar}} c_b(0) + \frac{2\pi U_{ba}(t) D^*(\omega_o - \omega_p)}{i\hbar} c_a(t) \end{aligned} \quad (2.16)$$

with

$$D(\omega, t) = \frac{1}{2\pi} \int_0^t e^{i\omega\tau} d\tau. \quad (2.17)$$

In deriving the result in (2.16), we have employed the slowly varying nature of the pulse shape U_p in (2.14), namely $U_{ab}(t') = U_{ab}(t)e^{-i\omega_p(t-t')}$.

As anticipated, the goal of the desired simplified treatment is the derivation of a set of semiclassical equations of motion for the level populations only. To this end, by employing the original set of equations (2.10) and by denoting the two level populations with f_a and f_b , it is easy to get the following result:

$$\frac{df_a}{dt} = \frac{d|c_a|^2}{dt} = 2\Re\left(\frac{U_{ab}(t)c_b(t)c_a^*(t)}{i\hbar}\right) = -\frac{d|c_b|^2}{dt} = -\frac{df_b}{dt}. \quad (2.18)$$

By assuming as initial condition the system ground state ($c_a(0) = 1, c_b(0) = 0$), replacing c_a and c_b with their first-order expansions (2.16), and considering terms up to second order in U_{ab} only, we finally obtain²

$$\begin{aligned} \frac{df_a}{dt} &= P_{ab}f_b - P_{ba}f_a \\ \frac{df_b}{dt} &= P_{ba}f_a - P_{ab}f_b \end{aligned} \quad (2.19)$$

with

$$P_{ab}(t) = P_{ba}(t) = \frac{2\pi}{\hbar^2} |U_{ab}|^2 F(\omega_o - \omega_p, t) \quad (2.20)$$

and

$$F(\omega, t) = D(\omega, t) + D^*(\omega, t) = \frac{1}{\pi} \int_0^t \cos(\omega\tau) d\tau = \frac{1}{\pi} \frac{\sin(\omega t)}{\omega}. \quad (2.21)$$

A few important comments are now in order. In spite of its Boltzmann-like structure (see (1.68)), the semiclassical result (2.19) does not constitute a genuine set of rate equations: The quantities in (2.20) are not positive-definite, and therefore they cannot be regarded as transition rates. Indeed, the function $F(\omega)$ in (2.21) is the result of a fully quantum-mechanical interference process, and – for any finite value of t – the latter will exhibit negative-value regions. However, for increasing values of time, such rapidly oscillating interference pattern will tend to a Dirac delta function, i.e.,

$$\lim_{t \rightarrow \infty} \frac{1}{\pi} \frac{\sin(\omega t)}{\omega} = \delta(\omega), \quad (2.22)$$

and the quantity P_{ab} in (2.20) reduces to the well-known Fermi's golden rule

$$P_{ab} = \frac{2\pi}{\hbar^2} |U_{ab}|^2 \delta(\omega_o - \omega_p) = \frac{2\pi}{\hbar} |U_{ab}|^2 \delta(\hbar\omega_o - \hbar\omega_p) : \quad (2.23)$$

² Within the general framework of a semiclassical treatment, here various first-order terms involving the interlevel phase coherence in (2.12) have been disregarded; the latter, in contrast, will play a central role for the description of nonlinear ultrafast optical processes (see below).

in the limit $t \rightarrow \infty$ – i.e., far from the initial condition – we recover a genuine transition probability per time unit proportional to the squared modulus of the interaction matrix element U_{ab} as well as to the energy-conserving Dirac delta function; it follows that in this longtime regime, typically referred to as completed-collision limit (see below), the semiclassical description in (2.19) is now fully equivalent to the semiclassical Boltzmann picture introduced in Sect. 1.3.

Figure 2.1 shows the interference pattern in (2.21) as a function of the so-called detuning energy $\hbar\omega$ at three different times: $t = 150$ fs, $t = 300$ fs, and $t = 600$ fs. Recalling that in our case the detuning energy ($\hbar\omega = \hbar(\omega_o - \omega_p)$) is just the difference between the interlevel energy splitting $\hbar\omega_o = \epsilon_b - \epsilon_a$ and the photon energy $\hbar\omega_p$, the scenario depicted in Fig. 2.1 clearly shows that at short times (after the state preparation) one deals with the so-called energy-nonconserving transitions (see, e.g., [108]), i.e., transitions characterized by a non-zero detuning energy $\hbar\omega^3$: Indeed, immediately after the state

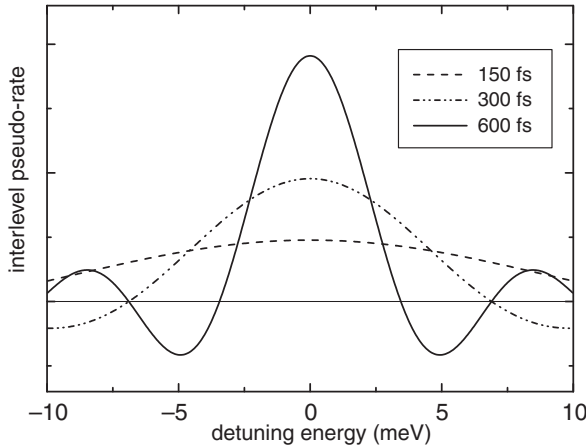


Fig. 2.1. Interference pattern (2.21) as a function of the detuning energy $\hbar\omega$ at three different times: $t = 150$ fs, $t = 300$ fs, and $t = 600$ fs. This scenario clearly shows that at short times (after the state preparation) one deals with the so-called energy-nonconserving transitions, i.e., transitions characterized by a non-zero detuning energy $\hbar\omega$: Indeed, immediately after the state preparation ($t = 150$ fs) we deal with an extremely broad profile; for increasing values of time ($t = 300$ fs) we assist to the progressive formation of an energy-conserving resonance peak ($\hbar\omega = 0$) accompanied by negative tails; at longer times ($t = 600$ fs) we are left with a much sharper central peak surrounded by an oscillatory behavior, which can be regarded as a precursor of the Dirac delta function obtained in the limit $t \rightarrow \infty$

³ The presence of electron–phonon energy-nonconserving transitions in photoexcited semiconductors, originally pointed out in 1989 by Carlo Jacoboni and co-workers [108], has been experimentally demonstrated by Alfred Leitenstorfer and co-workers in 1997 [109].

preparation ($t = 150$ fs) we deal with an extremely broad profile; for increasing values of time ($t = 300$ fs) we assist to the progressive formation of an energy-conserving resonance peak ($\hbar\omega = 0$) accompanied by negative tails; at longer times ($t = 600$ fs) we are left with a much sharper central peak surrounded by an oscillatory behavior, which can be regarded as a precursor of the Dirac delta function obtained in the limit $t \rightarrow \infty$. From our analysis it is easy to recognize the typical features of the time-energy uncertainty relation governing this quantum-mechanical interaction process: At very short times we deal with a significant uncertainty of our transition energy, which implies that immediately after the state preparation the electron may undergo transitions from state a to state b induced by non-resonant photons; for increasing values of time such energy-nonconserving transitions become less and less important, and in the longtime limit we deal with energy-conserving processes only. This leads to the natural conclusion that for the present case the concept of collision-duration time introduced in the previous section coincides with the measurement time t for which energy-nonconserving transitions exceeding a given energy uncertainty $\delta\epsilon$ may be safely neglected.

A second crucial point needs to be addressed now. According to the analysis presented so far, on the one hand, in the longtime limit Fermi's golden rule (2.23) will induce energy-conserving processes only; on the other hand, at short times (immediately after the state preparation) the semiclassical equations (2.19) may allow for energy-nonconserving transitions. It is thus crucial to understand if such short-time energy-nonconserving processes will also influence the state populations at longer times. To this end, let us evaluate the probability of finding our electron in the excited state b at time t ; by neglecting higher-order contributions (in P_{ab}), such occupation probability is simply given by the time integral of P_{ab} :

$$f_b(t) = \int_0^t P_{ab}(t') dt' . \quad (2.24)$$

Recalling the explicit form of P_{ab} in (2.20) and the slowly varying character of our excitation, the final result is

$$f_b(t) \propto \int_0^t F(\omega, t') dt' = \frac{2}{\pi} \frac{\sin^2\left(\frac{1}{2}\omega t\right)}{\omega^2} . \quad (2.25)$$

Figure 2.2 shows the excited-level occupation f_b in (2.25) as a function of the detuning energy $\hbar\omega$ at the same three times considered in Fig. 2.1: $t = 150$ fs, $t = 300$ fs, and $t = 600$ fs. As expected, at very short times we have a significant excited-level occupation also for non-zero detuning energies, a clear fingerprint of energy-nonconserving processes; however, for increasing times the excited-level occupation displays the progressive formation of an energy-conserving resonance peak accompanied again by oscillatory tails; at longer times we are left with a much sharper central peak, which can be regarded again as a precursor of a Dirac delta-like behavior obtained in the limit

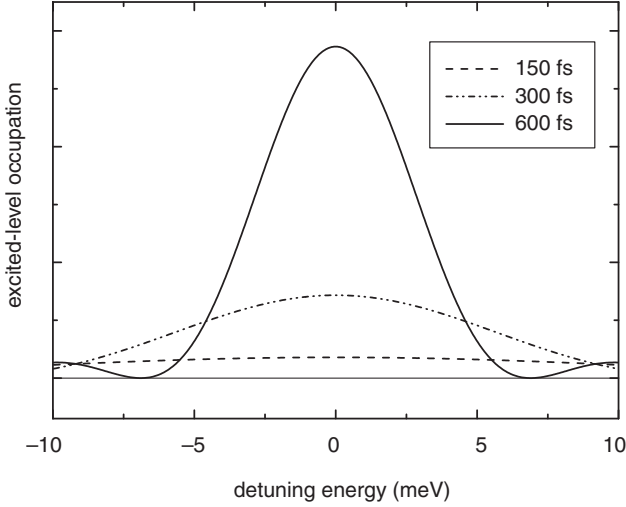


Fig. 2.2. Excited-level occupation f_b in (2.25) as a function of the detuning energy $\hbar\omega$ at the same three times considered in Fig. 2.1: $t = 150$ fs, $t = 300$ fs, and $t = 600$ fs. At very short times we have a significant excited-level occupation also for non-zero detuning energies, a clear fingerprint of energy-nonconserving processes; however, for increasing times the excited-level occupation displays the progressive formation of an energy-conserving resonance peak accompanied again by oscillatory tails; at longer times we are left with a much sharper central peak, which can be regarded again as a precursor of a Dirac delta-like behavior

$t \rightarrow \infty$. The scenario depicted in Fig. 2.2 tells us that – in spite of energy-nonconserving processes at short times – the longtime level occupation does not exhibit significant signatures of such ultrafast dynamics; indeed, as discussed in [110], it is possible to show that these ultrafast non-resonant electronic excitations are subsequently canceled by corresponding non-resonant stimulated-emission processes (see negative tails in Fig. 2.1), so that the longtime result does not show any energy-conservation violation. As we shall see, this is true provided that our quantum-mechanical interference process is not disturbed by other ultrafast interaction mechanisms.

In summary, we have seen that for weak as well as slowly varying optical excitations, both ultrafast and longtime level occupations are properly described by the semiclassical Boltzmann-like equations (2.19). More specifically, while in the ultrafast regime it is crucial to include energy-nonconserving processes via the transition pseudo-rate (2.20), for longtime investigations the latter may be safely replaced by the conventional transition rates given by Fermi's golden rule in (2.23). It follows that in spite of the purely quantum-mechanical character of the original set of equations (2.10), for slowly varying excitations and long times the latter may be replaced by a fully semiclassical set of Boltzmann-like equations, describing the light–matter interaction via purely stochastic scattering processes (see, e.g., [28]).

Let us finally consider the case of an ultrafast optical excitation characterized by a spectral function $\tilde{U}(\omega)$, i.e.,

$$U_{ab}(t) = \int \tilde{U}(\omega) e^{i\omega t} d\omega . \quad (2.26)$$

Assuming again to work within the weak-excitation regime ($|U_{ab}(t)| \ll \hbar\omega_o$), the set of equations (2.16), corresponding to a slowly varying excitation, in this case should be replaced by

$$\begin{aligned} c_a(t) &= e^{-\frac{i\epsilon_a t}{\hbar}} c_a(0) + \frac{2\pi\bar{U}(\omega_o, t)}{i\hbar} e^{i\omega_o t} c_b(t) \\ c_b(t) &= e^{-\frac{i\epsilon_b t}{\hbar}} c_b(0) + \frac{2\pi\bar{U}^*(\omega_o, t)}{i\hbar} e^{-i\omega_o t} c_a(t) \end{aligned} \quad (2.27)$$

with

$$\bar{U}(\omega_o, t) = \frac{1}{2\pi} \int_0^t U_{ab}(t') e^{-i\omega_o t'} dt' . \quad (2.28)$$

By inserting these new solutions into (2.18) and considering again terms up to second order in U_{ab} only, it is possible to obtain again the set of Boltzmann-like equations (2.19) with new pseudo-rates given by

$$P_{ab}(t) = P_{ba}(t) = \frac{4\pi}{\hbar^2} \Re (U_{ba}(t) e^{i\omega_o t} \bar{U}(\omega_o, t)) . \quad (2.29)$$

Also in this case, it is possible to show that – similar to the slowly varying-excitation result in (2.20) – at short times the system will exhibit energy-nonconserving transitions. The crucial question is now if such an ultrafast excitation will lead to energy-conservation violations also in the longtime limit. To this end, let us consider again the probability of finding our electron in the excited state b at time t ; by inserting the pseudo-rate (2.29) into (2.24), the final result is

$$f_b(t) \propto \int_0^t dt' 2\Re (U_{ba}(t') e^{i\omega_o t'} \bar{U}(\omega_o, t')) \propto |\bar{U}(\omega_o, t)|^2 , \quad (2.30)$$

i.e., the probability of finding our electron in the excited state at time t is proportional to the squared modulus of the function \bar{U} in (2.28); the latter, in turn, depends crucially on the duration as well as on the central time of the optical pulse in (2.26). In particular, for ultrafast excitations fully contained within our time interval ($0 < t' < t$), the time integral in (2.28) may be extended from $-\infty$ to $+\infty$, and thus in this case the function \bar{U} coincides with the pulse spectral function \tilde{U} in (2.26), i.e., with the Fourier transform of the original ultrafast excitation. It follows that when the pulse is fully contained in our time interval, we are in the completed-collision limit previously mentioned, and the final electron occupation is determined by the pulse Fourier transform only; in contrast, for observation times t comparable to or shorter

than the pulse duration, the electron population will display additional energy broadening due to short-time energy-nonconserving transitions.

In order to better elucidate the scenario previously discussed, let us consider, as prototypical example of ultrafast excitation, a Gaussian optical pulse

$$U_{ab}(t) = U_o e^{-\left(\frac{t-t_0}{2\tau_p}\right)^2} e^{i\omega_p t} \quad (2.31)$$

with central photon energy $\hbar\omega_p$, central time t_0 , and pulse duration τ_p . Figure 2.3 shows the excited-level occupation (2.30) as a function of the detuning energy $\hbar\omega = \hbar\omega_p - \hbar\omega_o$ at different observation times for a Gaussian pulse of duration $\tau_p = 100$ fs and central time $t_0 = 200$ fs. As expected, at early stages ($t = 100$ fs) we observe an extremely broad electron distribution due to energy-nonconserving processes; for increasing times ($t = 200$ fs and $t = 300$ fs) such energy broadening is progressively reduced, and close to the end of our excitation ($t = 400$ fs) the latter approaches the square of the excitation Fourier transform, which for our Gaussian pulse is Gaussian as well

$$|\tilde{U}(\omega)|^2 \propto e^{-\frac{(\hbar\omega)^2}{2\Delta\epsilon^2}}, \quad (2.32)$$

with $\Delta\epsilon = \frac{\hbar}{2\tau_p} \sim 3$ meV.

We are then led to the conclusion that opposite to the case of a slowly varying excitation, the application of an ultrafast optical pulse gives rise to a longtime electronic energy broadening, which is just a fingerprint of the spectral broadening of our time-dependent excitation. Indeed, we deal with

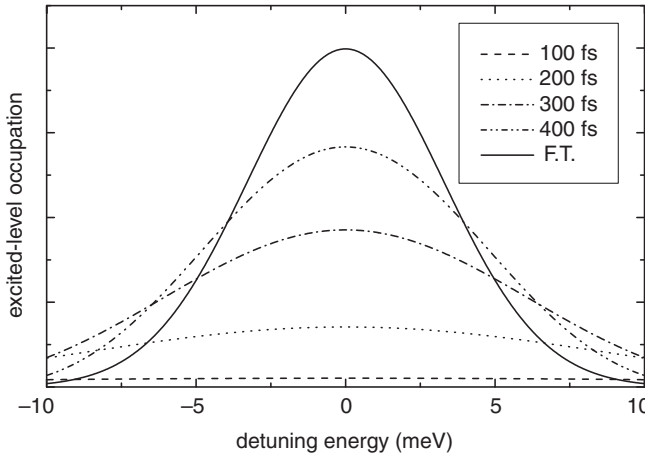


Fig. 2.3. Excited-level occupation (2.30) as a function of the detuning energy $\hbar\omega = \hbar\omega_p - \hbar\omega_o$ at different observation times for a Gaussian pulse of duration $\tau_p = 100$ fs and central time $t_0 = 200$ fs. At early stages ($t = 100$ fs) we observe an extremely broad electron distribution due to energy-nonconserving processes; for increasing times ($t = 200$ fs and $t = 300$ fs) such energy broadening is progressively reduced, and close to the end of our excitation ($t = 400$ fs) the latter approaches the square of the excitation Fourier transform

a sort of superposition principle: The ultrafast pulse (2.26) may always be regarded as a coherent superposition of monochromatic components with different photon energies; each of these components at long times will result in electron–photon energy-conserving processes, then producing an overall energy broadening described by $|\tilde{U}(\omega)|^2$. As we shall discuss in more detail in Chaps. 9 and 10, the above time–energy uncertainty relation between pulse duration and electronic energy broadening, i.e.,

$$\Delta\epsilon\tau_p \geq \frac{\hbar}{2} , \quad (2.33)$$

constitutes one of the most severe limitations in the design and optimization of ultrafast electro-optical quantum devices.

So far, we have limited our attention to the case of weak optical excitations; within our two-level picture this means that the excited-state occupation in (2.25) as well as (2.30) is always very small ($f_b(t) \ll 1$). In order to describe light–matter interaction induced by strong optical pulses, the perturbative scheme previously considered – as well as the resulting semiclassical equations (2.19) – is definitely inadequate. Moreover, the interlevel quantum-mechanical phase coherence is not affecting the level populations $f_a = |c_a|^2$ and $f_b = |c_b|^2$ (see (2.11) and (2.13)); in contrast, the latter is well described via the quantity $p = c_b c_a^*$ in (2.12) also called interlevel polarization (see below). It is then clear that in order to describe phase-sensitive ultrafast experiments induced by strong optical excitations, we need to replace the semiclassical equations (2.19) with a new set of equations involving the interlevel polarization as well. More specifically, combining the original equations of motion (2.10) with the definitions of the level occupations f_a and f_b as well as of the interlevel polarization p , we get

$$\begin{aligned} \frac{df_a}{dt} &= 2\Re\left(\frac{U_{ab}p}{i\hbar}\right) = -\frac{df_b}{dt} \\ \frac{dp}{dt} &= \frac{\epsilon_b - \epsilon_a}{i\hbar}p + \frac{U_{ba}}{i\hbar}(f_a - f_b) . \end{aligned} \quad (2.34)$$

The latter are known as optical Bloch equations (see, e.g., [33, 90]) in analogy with the equations first derived by Felix Bloch in 1946 [111] for spin systems. They constitute the simplest application of the well-known density-matrix formalism (see, e.g., [112, 113]) presented in Chap. 3: Our new variables may be regarded as the elements of the following two-by-two matrix:

$$\hat{\rho} = \begin{pmatrix} \rho_{aa} & \rho_{ab} \\ \rho_{ba} & \rho_{bb} \end{pmatrix} = \begin{pmatrix} f_a & p^* \\ p & f_b \end{pmatrix} = \begin{pmatrix} c_a c_a^* & c_a c_b^* \\ c_b c_a^* & c_b c_b^* \end{pmatrix} . \quad (2.35)$$

This is the so-called density matrix for our two-level system; indeed, recalling that $c_a = \langle a|\psi\rangle$ and $c_b = \langle b|\psi\rangle$, the density matrix (2.35) may also be regarded as the operator

$$\hat{\rho} = |\psi\rangle\langle\psi| \quad (2.36)$$

written in our two-level basis. The operator in (2.36) – called density-matrix operator – in this particular case (corresponding to a so-called pure state [112, 113]) is simply given by the projector of the system state vector $|\psi\rangle$ (see (3.7) in Chap. 3).

Let us consider again the case of a continuous optical excitation resonant with our two-level system: $U_{ab}(t) = U_o e^{i\omega_o t}$. If we choose as initial condition at time $t = 0$ the system ground state ($\{f_a = 1, f_b = 0, p = 0\}$), the solution of the optical Bloch equations (2.34) is given by

$$\begin{aligned} f_a(t) &= \cos^2\left(\frac{1}{2}\omega_R t\right) \\ f_b(t) &= \sin^2\left(\frac{1}{2}\omega_R t\right) \\ p(t) &= \frac{1}{4} \left[e^{-i\omega^+ t} - e^{-i\omega^- t} \right] , \end{aligned} \quad (2.37)$$

where $\omega^\pm = \omega_o \pm \omega_R$. As anticipated, the above solution describes a Rabi oscillation regime. In particular, the interlevel density-matrix element p originates from the superposition of the two frequency components ω^+ and ω^- . They differ from ω_o by the Rabi frequency ω_R . Such modification of the two-level frequency ω_o due to its coupling with the external field is known as “Rabi splitting” (see, e.g., [114]). If we now rewrite the interlevel density-matrix element p in (2.37) as

$$p(t) = -\frac{i}{2} e^{-i\omega_o t} \sin(\omega_R t) , \quad (2.38)$$

we see that apart from the quantum-mechanical phase factor corresponding to the interlevel energy separation $\hbar\omega_o$, its amplitude exhibits Rabi oscillations according to $\sin(\omega_R t)$. More specifically, we have

$$|p|^2 \propto \sin^2(\omega_R t) \propto \cos^2\left(\frac{1}{2}\omega_R t\right) \sin^2\left(\frac{1}{2}\omega_R t\right) \propto f_a(t)f_b(t) , \quad (2.39)$$

i.e., the quantity $|p|^2$ is proportional to the product of the two occupation numbers, thus reflecting the total (or macroscopic) dipole moment of our two-level system at time t . This elucidates the link between optically induced phase coherence and polarization: A coherent optical excitation gives rise to a coherent quantum-mechanical superposition of the two states which results in a macroscopic polarization of the system. Such polarization field is fully described by the non-diagonal matrix element p in (2.38).⁴

⁴ It is important to stress that opposite to the Boltzmann-like treatment previously considered (see (2.19)), the optical Bloch equations (2.34) may describe light-induced population inversion ($f_b > f_a$) and therefore stimulated-emission coherent processes (see also Chap. 8).

The optical Bloch equations (2.34) and the Schrödinger equations (2.10) are totally equivalent; however, as we shall see, the density-matrix description allows, in addition to the study of coherent phenomena, for the analysis of incoherent phenomena, not possible within a simple Schrödinger-equation formalism.

As a matter of fact, the above simplified treatment of light-matter interaction – based on a single isolated two-level system – neglects any kind of incoherent – i.e., energy-dissipation as well as phase-breaking – phenomena induced by the host material; indeed, dealing with optically excited solid-state electrons, such incoherent processes will lead to a decay of the excited-state population as well as of the interlevel polarization, thus destroying the optically induced phase coherence previously discussed (see (2.12)). As anticipated, such incoherent phenomena may be easily incorporated within our simplified two-level system description via the optical-Bloch-equation scheme previously introduced; more specifically, the set of equations (2.34) may be generalized as

$$\begin{aligned}\frac{df_a}{dt} &= 2\Re\left(\frac{U_{ab}p}{i\hbar}\right) - \frac{f_a - f_a^\circ}{T_1} \\ \frac{df_b}{dt} &= -2\Re\left(\frac{U_{ab}p}{i\hbar}\right) - \frac{f_b - f_b^\circ}{T_1} \\ \frac{dp}{dt} &= \frac{\epsilon_b - \epsilon_a}{i\hbar}p + \frac{U_{ba}}{i\hbar}(f_a - f_b) - \frac{p}{T_2}.\end{aligned}\quad (2.40)$$

Here, the incoherent phenomena previously mentioned are accounted for via simple relaxation-time approximations: On the longtime limit, the level populations f_a and f_b tend to their thermal-equilibrium values f_a° and f_b° via a relaxation time T_1 , while the interlevel polarization p will decay to 0 according to a second relaxation time T_2 . The theoretical scheme in (2.40) is known as T_1/T_2 model (see, e.g., [33, 90]).

Let us consider again the ultrafast-excitation regime previously discussed (see (2.11)) and, in particular, the case of a $\frac{\pi}{4}$ pulse ($\alpha = \frac{\pi}{4}$) able to generate an after-pulse equipopulated coherent state: $f_a = f_b = \frac{1}{2}$, $p = -\frac{i}{2}$. In the limit $T_1 \gg T_2$ the population relaxation terms in (2.40) may be safely neglected, and the resulting interlevel polarization is simply given by

$$p(t) = p(0)e^{-i\omega_\circ t}e^{-\frac{t}{T_2}} \propto ie^{-i\omega_\circ t}e^{-\frac{t}{T_2}}. \quad (2.41)$$

In addition to the interlevel quantum-mechanical phase factor in (2.12), the presence of incoherent scattering sources manifests itself in a decay of the interlevel polarization described by the relaxation time T_2 . It follows that the overall polarization dynamics is the result of a non-trivial interplay between coherent and incoherent phenomena. More specifically, in the limit $\omega_\circ T_2 \gg 1$ – also referred to as coherent regime – the polarization decay is negligible on the interlevel time-scale ω_\circ^{-1} ; in contrast, in the limit $\omega_\circ T_2 \ll 1$ – also referred to

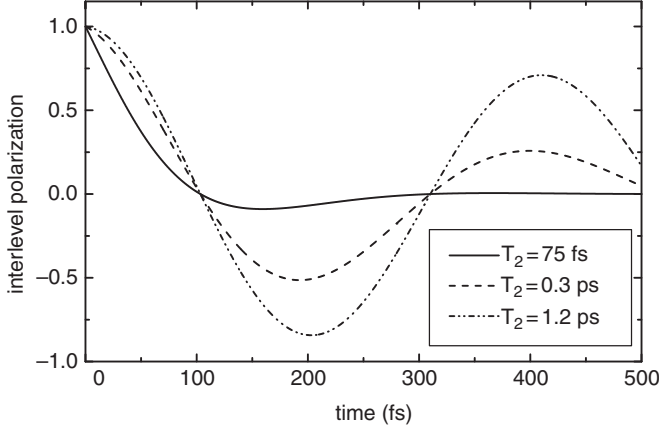


Fig. 2.4. Imaginary part of the interlevel polarization (2.41) corresponding to an interlevel energy splitting of 10 meV for three different values of the relaxation time T_2 : for $T_2 = 1.2$ ps, we have a nearly periodic oscillatory behavior confirming a coherent-like regime where the incoherent polarization decay plays a very minor role; for $T_2 = 75$ fs, we deal with an incoherent-like regime, characterized by a nearly exponential decay and by a corresponding suppression of the coherent oscillatory behavior; for $T_2 = 300$ fs, we deal with an intermediate regime characterized by a strong interplay between coherent oscillations and incoherent decay

as incoherent regime – coherent oscillations are totally dominated/suppressed by a polarization decay much faster than the interlevel time-scale.

To better illustrate the scenario discussed so far, in Fig. 2.4 we show the imaginary part of the interlevel polarization (2.41) corresponding to an interlevel energy splitting of 10 meV for three different values of the relaxation time T_2 : for $T_2 = 1.2$ ps, we have a nearly periodic oscillatory behavior confirming a coherent-like regime where the incoherent polarization decay plays a very minor role; in contrast, for $T_2 = 75$ fs, we deal with an incoherent-like regime, characterized by a nearly exponential decay and by a corresponding suppression of the coherent oscillatory behavior; finally, for $T_2 = 300$ fs, we deal with an intermediate regime characterized by a strong interplay between coherent oscillations and incoherent decay.

In this context, it is important to recall that the magnitude of the polarization decay in (2.41) may also be detected looking to the imaginary part of its Fourier transform, which in turn is proportional to the optical-absorption spectrum, i.e.,

$$A(\hbar\omega) \propto \Im \left(\int_0^\infty p(t') e^{i\omega t'} dt' \right) \propto \frac{\Gamma}{(\omega - \omega_0)^2 + \Gamma^2} . \quad (2.42)$$

Here, $\Gamma = \frac{\hbar}{T_2}$ is the energy broadening of the resulting Lorentzian spectral line, usually referred to as “homogeneous broadening.”

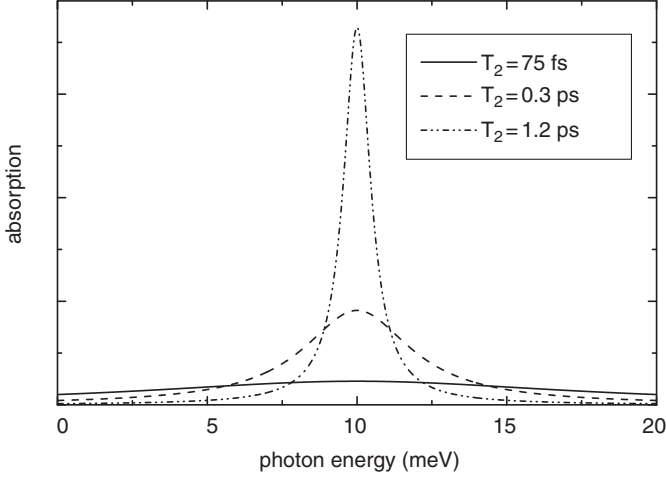


Fig. 2.5. Optical-absorption spectra corresponding to the three results of Fig. 2.4. For decreasing values of the decay time T_2 we observe an increase of the absorption line-width Γ (see (2.42))

Figure 2.5 shows the optical-absorption spectra corresponding to the three results of Fig. 2.4: As expected, for decreasing values of the decay time T_2 we observe an increase in the absorption line-width Γ .

As we shall discuss in the following section, while for the coherent as well as for the incoherent regime previously identified (see Fig. 2.4) the quantitative description of semiconductor devices may still be grounded on simplified – i.e., Schrödinger-like or semiclassical – models, any realistic simulation of the intermediate regime requires a fully microscopic approach able to treat on the same footing both coherent and incoherent phenomena.

Let us now discuss the extension of the simplified two-level description presented so far to the realistic case of a semiconductor crystal. As recalled in Sect. 1.2, a slowly varying optical excitation induces vertical transitions from a given occupied band $\nu = v$ (called valence band) to a given empty band $\nu = c$ (called conduction band); each of these transitions may be regarded as a two-level system formed by the Bloch states $\mathbf{k}v$ and $\mathbf{k}c$. It follows that, qualitatively speaking, our semiconductor crystal may be regarded as a collection of \mathbf{k} -dependent two-level systems driven by the same applied excitation. Indeed, by performing an heuristic and straightforward generalization of the optical Bloch equations (2.40), one gets

$$\begin{aligned} \frac{df_{\mathbf{k}v}}{dt} &= 2\Re\left(\frac{U_{\mathbf{k}}p_{\mathbf{k}}}{i\hbar}\right) - \frac{f_{\mathbf{k}v} - f_{\mathbf{k}v}^{\circ}}{T_1} \\ \frac{df_{\mathbf{k}c}}{dt} &= -2\Re\left(\frac{U_{\mathbf{k}}p_{\mathbf{k}}}{i\hbar}\right) - \frac{f_{\mathbf{k}c} - f_{\mathbf{k}c}^{\circ}}{T_1} \\ \frac{dp_{\mathbf{k}}}{dt} &= \frac{\epsilon_{\mathbf{k}c} - \epsilon_{\mathbf{k}v}}{i\hbar}p_{\mathbf{k}} + \frac{U_{\mathbf{k}}^*}{i\hbar}(f_{\mathbf{k}v} - f_{\mathbf{k}c}) - \frac{p_{\mathbf{k}}}{T_2}, \end{aligned} \quad (2.43)$$

where the \mathbf{k} -dependent coupling energies $U_{\mathbf{k}}$ are proportional to the dipole matrix elements $p_{\mathbf{k},cv}$ in (1.27). Indeed, the above result is the simplest version of the so-called semiconductor Bloch equations (see, e.g., [33, 90, 115]), i.e., the generalization to semiconductors of the optical Bloch equations (2.40) originally introduced for the study of atomic and molecular systems. Again, the new set of variables, given by the Bloch-state occupations $f_{\mathbf{k}v}$ and $f_{\mathbf{k}c}$ as well as by the interband ($v \rightarrow c$) microscopic polarizations $p_{\mathbf{k}}$, correspond to well precise elements of the electronic density matrix written in the Bloch basis: Similar to the two-level-system case in (2.35), the Bloch-state occupations correspond to diagonal elements ($f_{\mathbf{k}v} = \rho_{\mathbf{k}v,\mathbf{k}v}$ and $f_{\mathbf{k}c} = \rho_{\mathbf{k}c,\mathbf{k}c}$), while the interband polarizations correspond to non-diagonal matrix elements ($p_{\mathbf{k}} = \rho_{\mathbf{k}c,\mathbf{k}v}$), thus describing the interband quantum-mechanical phase coherence. The meaning and role of diagonal versus non-diagonal density-matrix elements will be discussed in more detail in Chap. 3.

In order to better illustrate the main differences between the single two-level system and the semiconductor crystal, let us consider again the ultrafast-optical-excitation regime in (2.41), whose semiconductor version is given by

$$p_{\mathbf{k}}(t) = p_{\mathbf{k}}(0)e^{-i\omega_{\mathbf{k}}t}e^{-\frac{t}{T_2}} , \quad (2.44)$$

where $\hbar\omega_{\mathbf{k}} = \epsilon_{\mathbf{k}c} - \epsilon_{\mathbf{k}v}$ denotes the interband energy difference. This tells us that within such model, for any \mathbf{k} value, we deal with an interband microscopic polarization characterized by a constant decay time T_2 and by a \mathbf{k} -dependent rotation frequency $\omega_{\mathbf{k}}$. As discussed in [110], it is possible to show that conventional optical experiments are not able to detect such microscopic polarizations individually; in contrast, the measured quantity is the total polarization p^{tot} induced by our optical excitation, i.e.,

$$p^{\text{tot}}(t) = \sum_{\mathbf{k}} U_{\mathbf{k}} p_{\mathbf{k}}(t) . \quad (2.45)$$

By neglecting the \mathbf{k} -dependence of the dipole matrix element, the above total polarization will be of the form.

$$p^{\text{tot}}(t) \propto i \sum_{\mathbf{k}} e^{-i\omega_{\mathbf{k}}t} e^{-\frac{t}{T_2}} . \quad (2.46)$$

To elucidate the main features of the total-polarization dynamics, Fig. 2.6 shows the modulus of the total polarization (2.46) as a function of time for the same three T_2 values considered in Fig. 2.4; here, a simplified parabolic-band GaAs bulk model has been employed. As we can see, in spite of the relatively different T_2 values, the ultrafast polarization dynamics (i) is nearly T_2 independent and (ii) is decaying on a much faster time-scale. In order to understand this peculiar feature, it is useful to rewrite the total polarization (2.46) as

$$p^{\text{tot}}(t) \propto i e^{-\frac{t}{T_2}} f_p(t) \quad (2.47)$$

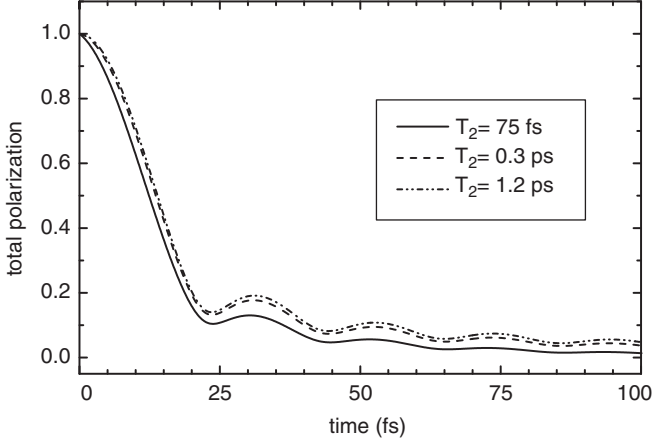


Fig. 2.6. Modulus of the total polarization (2.46) as a function of time for the same three T_2 values considered in Fig. 2.4; here, a simplified parabolic-band GaAs bulk model has been employed. In spite of the relatively different T_2 values, the ultrafast polarization dynamics is nearly T_2 independent and is decaying on a much faster time-scale (see text)

with

$$f_p(t) = \sum_{\mathbf{k}} e^{-i\omega_{\mathbf{k}}t} . \quad (2.48)$$

While at the initial time ($t = 0$) all the quantum-mechanical phase factors in (2.48) sum up constructively, for increasing times the latter will start to rotate with different frequencies, leading to a destructive-interference dynamics on a time-scale much shorter than the individual microscopic-polarization decay T_2 ; such phenomenon is usually referred to as polarization dephasing.

Such basic difference between individual and total-polarization decay manifests itself also via the corresponding absorption response; indeed, by evaluating the imaginary part of the Fourier transform of the total polarization in (2.46), one gets

$$A^{\text{tot}}(\hbar\omega) \propto \Im \left(\int_0^\infty p^{\text{tot}}(t') e^{i\omega t'} dt' \right) \propto \sum_{\mathbf{k}} \frac{\Gamma}{(\omega - \omega_{\mathbf{k}})^2 + \Gamma^2} . \quad (2.49)$$

As we can see, the total absorption $A^{\text{tot}}(\hbar\omega)$ is the sum of several Lorentzian peaks with different central frequencies $\omega_{\mathbf{k}}$. Recalling that in the limit $\Gamma \rightarrow 0$ the latter behave as Dirac delta functions, the total absorption (2.49) is qualitatively proportional to the J-DOS (1.30), which is fully consistent with the general result in (1.29). This shows that opposite to the previous single two-level case, the energetic broadening displayed by the total absorption – commonly referred to as “inhomogeneous broadening” – is basically a fingerprint of the system J-DOS, which is typically much larger than the individual Lorentzian line-width Γ .

The scenario reported in Fig. 2.6 tells us that conventional optical-absorption experiments – able to detect the total polarization in (2.45) – are not able to access the microscopic polarizations in (2.44); to this end, as discussed in detail in [90], it is necessary to adopt more refined ultrafast-optical-spectroscopy techniques based on many-pulse sequences, like, e.g., photon-echo experiments (see Sect. 2.5). This is indeed one of the most severe limitations of solid-state optics compared to atomic as well as molecular systems.

At this point it is imperative to notice that the semiconductor Bloch equations (2.43) – introduced as heuristic generalization of the simple two-level case in (2.40) – describe both electron–environment and electron–electron coupling via the T_1/T_2 phenomenological model previously mentioned. As discussed in detail in [110], a proper account of carrier–carrier as well as carrier–phonon interactions shows that, in addition to more refined incoherent-dynamics contributions, one deals with coherent quantum-mechanical corrections to the basic light–matter dynamics in (2.43), leading, e.g., to Hartree–Fock as well as polaronic renormalization effects. It follows that a rigorous (i.e., non-phenomenological) treatment of ultrafast optical excitations in semiconductors requires fully microscopic treatments far beyond the T_1/T_2 model in (2.43).

As a very final step, let us briefly discuss the extension of the phenomenological semiconductor Bloch equations (2.43) to the case of a semiconductor nanostructure. As shown in Chap. 3, a microscopic treatment of electro-optical processes in semiconductor nanomaterials requires a fully quantum-mechanical many-body approach; the latter is commonly based on an effective set of equations for the relevant single-particle density-matrix elements. More specifically, by denoting with α the generic electronic state of our semiconductor nanostructure, it is possible to show that the nanostructure generalization of the semiconductor Bloch equations (2.43) is always of the form

$$\frac{d\rho_{\alpha\alpha'}}{dt} = \left. \frac{d\rho_{\alpha\alpha'}}{dt} \right|_{1e} + \left. \frac{d\rho_{\alpha\alpha'}}{dt} \right|_{mb}, \quad (2.50)$$

i.e., the global time evolution of the density-matrix element $\rho_{\alpha\alpha'}$ is given by a one-electron (1e) contribution, describing the electronic dynamics in the presence of our electro-optical excitation, plus a many-body (mb) contribution, describing electron–electron as well as various electron–quasiparticle couplings (e.g., carrier–phonon, carrier–plasmon). While the first term may be treated exactly, the second one is treated within some approximation scheme.

By recalling that for the case of a semiconductor nanostructure, an optical excitation – according to its spectral range – may induce transitions between different electronic bands (interband transitions) or within the same band (intraband transitions), it follows that the relevant elements of the electronic density matrix involved depend crucially on the excitation spectral range. More specifically, by employing the envelope-function picture introduced in Sect. 1.2.2 we have $\alpha \equiv \nu, \bar{\alpha} \equiv \nu, \mathbf{k}_{\parallel} n$, i.e., the generic envelope-function state α is specified by its band index ν plus its envelope-function index $\bar{\alpha}$

(see (1.41)); the latter depends on the nanostructure dimensionality D and is given by the parallel-subspace wavevector \mathbf{k}_{\parallel} and by the corresponding subband index n (see (1.43)). It follows that in addition to the state populations corresponding to the diagonal density-matrix elements ($f_{\alpha} = \rho_{\alpha\alpha}$), for intraband ($\nu = \nu'$) excitations the only relevant quantities are given by intraband polarizations $p_{\nu\mathbf{k}_{\parallel},nn'}^{\text{intra}}$ corresponding to the non-diagonal density-matrix elements $\rho_{\nu\mathbf{k}_{\parallel}n,\nu\mathbf{k}_{\parallel}n'}$; the latter are also referred to as intersubband ($n \rightarrow n'$) polarizations. In contrast, for interband ($\nu \neq \nu'$) excitations the only relevant quantities are given by interband polarizations $p_{\mathbf{k}_{\parallel},\nu n,\nu' n'}^{\text{inter}}$ corresponding to the non-diagonal density-matrix elements $\rho_{\nu\mathbf{k}_{\parallel}n,\nu'\mathbf{k}_{\parallel}n'}$; the latter describe interband optical transitions connecting the generic subband n in band ν with the generic subband n' in band ν' . Compared to the original semiconductor Bloch equations (2.43), moving from bulk to nanostructures the three-dimensional wavevector \mathbf{k} is replaced by the parallel-subspace wavevector \mathbf{k}_{\parallel} , while – in addition to the band index – the subband index n should be considered as well.

As we shall discuss extensively in the following chapters, the approximation level employed for the description of the many-body contribution in (2.50) depends crucially on the specific problem under investigation; generally speaking, we shall adopt specific perturbation expansions combined with corresponding adiabatic-decoupling schemes. In particular, for slowly varying electro-optical excitations in the longtime regime, it is possible to show that all non-diagonal density-matrix elements may be adiabatically eliminated, leaving as relevant variables the electronic-state populations f_{α} of the conventional semiclassical picture introduced in Sect. 1.3. It follows that in this limit the nanostructure version of the semiconductor Bloch equations (2.50) reduces to the Boltzmann-like equation (1.73), where the light–matter interaction may be treated stochastically via corresponding intra- as well as interband transition probabilities $P_{\alpha\alpha'}$. This suggests that the semiclassical picture is just a limiting case of the density-matrix formalism presented in Chap. 3.

As a final remark, let us discuss the concept of phase coherence in connection with the choice of representation. On the basis of the density-matrix picture – whose general formulation will be given in the following chapter – the quantum-mechanical phase coherence is described by the non-diagonal density-matrix elements $\rho_{\alpha\alpha'}$ in (2.50). However, this separation in diagonal versus non-diagonal terms is clearly representation dependent: what is diagonal in a given basis is in general non-diagonal in a different basis and vice versa. Indeed, if one considers, as basis set, the eigenstates of the global Hamiltonian (describing system plus electro-optical excitation), the density matrix written in this new basis is always diagonal, i.e., no phase coherence. Thus, in order to speak of optically induced phase coherence, we need to regard the global Hamiltonian as the sum of the system Hamiltonian plus an external driving-force term (see (2.6)). Provided such separation between system-of-interest and driving force, the non-diagonal density-matrix elements within the representation given by the system eigenstates will describe the degree of

quantum-mechanical phase coherence induced on the system by the driving force.

As anticipated, in a semiconductor material we deal with a variety of many-body effects, not described/included in the usual Bloch state picture α ; it follows that the many-body term in (2.50) induces, in general, a sort of phase coherence $\rho_{\alpha\alpha'}$ between the single-particle Bloch states α and α' . Such a coherent phenomenon is obviously fictitious and is simply ascribed to the fact that the Bloch state basis differs from the rigorous eigenstates of the full many-body semiconductor Hamiltonian. Two typical examples of such fictitious phase coherence may help in clarifying this point.

The first case, discussed in Chap. 9, is that of Coulomb-induced phase coherence: Within a Coulomb-free representation, even at the simplest Hartree–Fock level, Coulomb interaction induces phase coherence between Coulomb-free states. This is clearly not the case within an excitonic basis (see (1.58)), where the density matrix is always diagonal.

The second and more intriguing case, discussed in Sect. 3.4, is that of a semiconductor superlattice in the presence of a constant and homogeneous electric field (see, e.g., [32]). As we shall see, in this case we deal with two physically equivalent representations (simply connected by a gauge transformation) leading to different descriptions of transport phenomena: Within the so-called Wannier–Stark representation the Bloch-oscillation dynamics is the result of phase coherence between the various Wannier–Stark states; in contrast, within the accelerated Bloch-state representation the same phenomenon is purely described on a semiclassical level in terms of carrier populations, i.e., no off-diagonal density-matrix elements.

2.3 Space-Dependent Phenomena

The discussion presented so far has been intentionally restricted to the case of slowly varying electro-optical excitations. In this case, the neglect of the photon momentum – also referred to as dipole approximation – leads to the vertical-transition picture previously introduced; indeed, according to the semiconductor Bloch equation (2.43), a slowly varying optical excitation creates a quantum-mechanical phase coherence between valence and conduction Bloch states characterized by the same wavevector \mathbf{k} – expressed by the interband polarization $p_{\mathbf{k}}$ – which, in turn, leads to after-pulse populations $f_{\mathbf{k}v}$ and $f_{\mathbf{k}c}$. As anticipated, such kinetic variables correspond to interband and intra-band density-matrix elements, always diagonal in \mathbf{k} : $f_{\mathbf{k}v/c} = \rho_{\mathbf{k}v/c, \mathbf{k}v/c}$ and $p_{\mathbf{k}} = \rho_{\mathbf{k}c, \mathbf{k}v}$. As discussed in more detail in [110], given a generic electronic-state basis α , the electron spatial density may be easily expressed in terms of the density matrix $\rho_{\alpha\alpha'}$ previously introduced according to

$$n(\mathbf{r}) = \sum_{\alpha\alpha'} \rho_{\alpha\alpha'} \psi_{\alpha}(\mathbf{r}) \psi_{\alpha'}^*(\mathbf{r}) . \quad (2.51)$$

For the particular case of the two-band model of the semiconductor Bloch equations (2.43), we get

$$n(\mathbf{r}) = \sum_{\mathbf{k}} [f_{\mathbf{k}v} |\phi_{\mathbf{k}v}(\mathbf{r})|^2 + f_{\mathbf{k}c} |\phi_{\mathbf{k}c}(\mathbf{r})|^2 + 2\Re(p_{\mathbf{k}} \phi_{\mathbf{k}c}(\mathbf{r}) \phi_{\mathbf{k}v}^*(\mathbf{r}))] . \quad (2.52)$$

In view of the periodicity properties of the conventional Bloch states $\phi_{\mathbf{k}\nu}$ in (1.8), the electronic spatial density (2.52) is always periodic, thus extending over the whole semiconductor crystal; this is indeed consistent with the assumption of a slowly varying, i.e., nearly constant, electromagnetic excitation.

Let us now consider the problem of a spatially localized excitation. In this case, opposite to the conventional semiconductor Bloch equations (2.43), it is possible to show that such an optical excitation induces diagonal ($\mathbf{k} = \mathbf{k}'$) as well as non-diagonal ($\mathbf{k} \neq \mathbf{k}'$) interband polarizations $p_{\mathbf{k}\mathbf{k}'} = \rho_{\mathbf{k}c, \mathbf{k}'v}$, giving rise to diagonal as well as non-diagonal valence and conduction density-matrix elements $f_{\mathbf{k}\mathbf{k}'}^v = \rho_{\mathbf{k}v, \mathbf{k}'v}$ and $f_{\mathbf{k}\mathbf{k}'}^c = \rho_{\mathbf{k}c, \mathbf{k}'c}$. Therefore, for the case of a spatially localized excitation the electron density (2.52) should be replaced by

$$n(\mathbf{r}) = \sum_{\mathbf{k}\mathbf{k}'} [f_{\mathbf{k}\mathbf{k}'}^v \phi_{\mathbf{k}v}(\mathbf{r}) \phi_{\mathbf{k}'v}^*(\mathbf{r}) + f_{\mathbf{k}\mathbf{k}'}^c \phi_{\mathbf{k}c}(\mathbf{r}) \phi_{\mathbf{k}'c}^*(\mathbf{r}) + 2\Re(p_{\mathbf{k}\mathbf{k}'} \phi_{\mathbf{k}c}(\mathbf{r}) \phi_{\mathbf{k}'v}^*(\mathbf{r}))] . \quad (2.53)$$

Contrary to the result in (2.52), due to non-vertical ($\mathbf{k} \neq \mathbf{k}'$) contributions, the electron spatial density (2.53) is not periodic anymore; in particular, it is possible to show that the latter exhibits the same spatial localization of the applied optical excitation, a quite intuitive result. It follows that, also within a periodic crystal, a spatially localized excitation may produce a strongly nonhomogeneous charge distribution, whose after-pulse dynamics requires a non-vertical density-matrix formulation.

In a similar way, a slowly varying intraband excitation applied to a semiconductor nanostructure will induce intersubband polarizations, resulting in nonhomogeneous valence and conduction carrier densities. Indeed, as discussed previously, for the case of semiconductor nanostructures the time evolution of the electronic density matrix $\rho_{\alpha\alpha'}$ is governed by the semiconductor Bloch equations (2.50) which, in turn, allows us to evaluate the time evolution of the electronic spatial density $n(\mathbf{r})$ in (2.51).

According to the semiclassical picture introduced in Sect. 1.3, for space-scales compatible with the position-momentum uncertainty principle, such a space-dependent carrier dynamics is well described via the conventional Boltzmann transport theory; in contrast, on very short space-scales the semiclassical picture fails, and fully quantum-mechanical approaches are imperative. For a quantitative study of space-dependent phenomena it is then crucial to establish a direct link between the classical picture and the quantum-mechanical density-matrix formulation; this is realized by the well-known Wigner-function formalism (see, e.g., [85] and references therein) presented in Chap. 4.

The key ingredient of the Wigner formulation of quantum mechanics is the so-called Wigner function, i.e., a function – originally introduced by Eugene

Wigner in 1932 [116] – defined over the ordinary phase-space \mathbf{r}, \mathbf{p} as the following Weyl–Wigner transform of the single-particle density matrix:

$$f_W(\mathbf{r}, \mathbf{p}) = \sum_{\alpha\alpha'} \mathcal{W}_{\alpha\alpha'}(\mathbf{r}, \mathbf{p}) \rho_{\alpha\alpha'} \quad (2.54)$$

with

$$\mathcal{W}_{\alpha\alpha'}(\mathbf{r}, \mathbf{p}) = \int d^3r' \psi_\alpha \left(\mathbf{r} + \frac{\mathbf{r}'}{2} \right) \frac{e^{-\frac{i\mathbf{p}\cdot\mathbf{r}'}{\hbar}}}{(2\pi\hbar)^{\frac{3}{2}}} \psi_{\alpha'}^* \left(\mathbf{r} - \frac{\mathbf{r}'}{2} \right) . \quad (2.55)$$

Combining the above definition with the general expression for the electron spatial density (2.51), it is easy to verify that

$$n(\mathbf{r}) \propto \int f_W(\mathbf{r}, \mathbf{p}) d^3p , \quad (2.56)$$

i.e., the spatial density is proportional to the integral over \mathbf{p} of the Wigner function (2.54). In spite of the strong similarities with the classical phase-space picture, it is important to stress that, in general, the Wigner function (2.54) is not positive-definite, and therefore the latter does not allow for a probabilistic interpretation. However, for slowly varying (in space) optical excitations and confinement-potential profiles, the Wigner function (2.54) is always positive and is well described via effective semiclassical transport models. In contrast, as already pointed out, in the presence of ultrashort spatial confinement and/or strongly inhomogeneous optical excitations, the fully non-diagonal density-matrix formalism of the semiconductor Bloch equations (2.50) is imperative, giving rise to highly non-classical Wigner-function profiles.

As a final remark, it is important to stress the strong similarities between ultrashort time and space phenomena. On the one hand, for the case of ultrafast phenomena the semiclassical picture comes out to be highly inadequate, since in addition to state populations it is crucial to consider intraband as well as interband polarizations; the latter – describing quantum-mechanical interference phenomena among different energy states – give rise to the well-known time–energy uncertainty relation. However, in the presence of slowly varying excitations, the polarizations may be adiabatically eliminated (see, e.g., [110]) and – in spite of the quantum-mechanical nature of the problem – the electronic dynamics may be well described via effective semiclassical equations. On the other hand, in the presence of strongly localized excitations, in addition to electron populations, it is crucial to consider non-vertical ($\mathbf{k} \neq \mathbf{k}'$) density-matrix elements. The latter – describing quantum-mechanical interference among different momentum values – reflect the well-known position-momentum uncertainty relation. Again, for slowly varying perturbations (in space) all non-diagonal density-matrix elements may be adiabatically eliminated (see, e.g., [117]), and our space-dependent problem may be safely treated via effective Boltzmann equations.

2.4 Quantum Systems with Spatial Boundaries

The quantum-mechanical description presented so far applies to the so-called closed systems, i.e., semiconductor materials extending over the whole coordinate space \mathbf{r} . In contrast, as already pointed out in Sect. 1.4, a semiconductor device [79, 81–84] is typically an “open system,” i.e., a portion of material characterized by a well precise volume Ω_d and spatial boundaries \mathbf{r}^b acting as electric contacts. It follows that, generally speaking, the presence of spatial boundaries will induce modifications to the semiconductor-nanostructure Bloch equations (2.50), whose open-system version may be schematically written as

$$\frac{d\rho_{\alpha\alpha'}}{dt} = \frac{d\rho_{\alpha\alpha'}}{dt}\bigg|_{1e} + \frac{d\rho_{\alpha\alpha'}}{dt}\bigg|_{mb} + \frac{d\rho_{\alpha\alpha'}}{dt}\bigg|_b. \quad (2.57)$$

Here, the last term describes the effect on the time evolution of the density matrix $\rho_{\alpha\alpha'}$ induced by our spatial boundaries.

As discussed in great detail in Chap. 4, the incorporation of spatial boundary conditions within a quantum-mechanical framework is a highly non-trivial task. In view of the intrinsic space-dependent character of the problem under examination, the most natural strategy seems to move from the density-matrix formalism to the Wigner picture via the Weyl–Wigner transform (2.55), and then to apply to the Wigner function (2.54) the standard U boundary-condition scheme discussed in Appendix B. However, in spite of the formal similarity between semiclassical and Wigner pictures, it comes out that such conventional boundary-condition scheme is definitely not compatible with the non-local character of quantum mechanics, leading to highly non-physical results like, e.g., negative electronic spatial densities (see Sect. 4.2).

To overcome this severe limitation, two alternative strategies may be adopted: (i) properly designed projection techniques (see Sect. 4.3) allowing, still within an open-system density-matrix framework, to incorporate spatial boundary effects via generalized injection/loss contributions and (ii) simplified closed-system approaches (see Sect. 4.4) describing the device-environment coupling dynamics via properly designed particle-conserving scattering super-operators.

2.5 Experimental Techniques

The investigation of nonequilibrium carrier dynamics in optically excited semiconductors started in the late 1960s with the analysis of the energy-relaxation process (see, e.g., [118]) by using continuous-wave excitation. The measurement of the carrier temperature as a function of the laser intensity – obtained from the luminescence spectrum – gave insight into the power loss from the carriers to the lattice, i.e., about carrier–phonon scattering processes. In subsequent years, these investigations were extended to different materials and excitation conditions. While band-to-band luminescence spectra gave only a

combination of electron and hole temperatures (see, e.g., [90]), direct information on the electronic distribution function was obtained by studying band-to-acceptor luminescence spectra of doped semiconductors (see, e.g., [119]).

However, as anticipated, only by using a pulsed excitation, dynamical processes can be directly investigated. Here, the pulse duration limits the temporal resolution and therefore restricts the phenomena which can be studied. The typical time-scales for many of the processes discussed in this book are in the range between a few femtoseconds and a few picoseconds. Therefore, the application of time-resolved nonlinear optical spectroscopy to the study of dynamical processes in semiconductors has been strongly linked to the ability of producing laser pulses on these time-scales. Such laser sources became available for semiconductor studies in the late 1970s (see, e.g., [120]). Since then a great number of phenomena have been studied, first mainly focusing on incoherent dynamics, i.e., the nonequilibrium dynamics of distribution functions, and subsequently analyzing more and more coherent phenomena, i.e., the dynamics of optically created interband and intraband polarizations.

A typical scenario for the dynamics of carrier distribution functions is plotted schematically in Fig. 2.7: The laser pulse with a given photon energy and a certain spectral width determined by its duration creates electron-hole pairs in a more or less localized region in \mathbf{k} -space. This initial distribution then relaxes due to the presence of scattering processes. In polar semiconductors on ultrafast time-scales there are typically two mechanisms of particular importance: Due to the polar coupling to longitudinal optical (LO) phonons

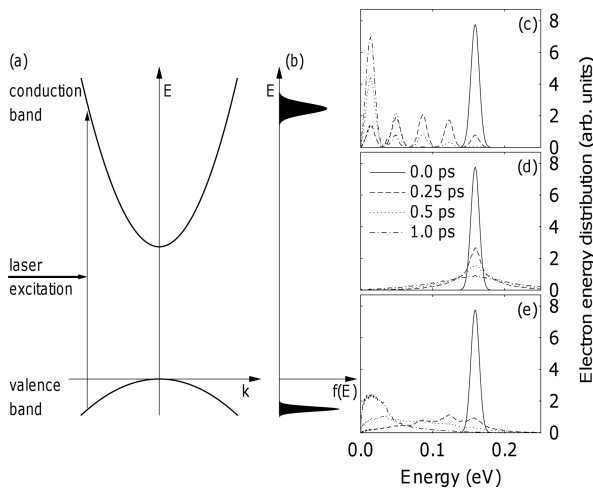


Fig. 2.7. Schematic plot of (a) the excitation process by a short laser pulse with a certain excess energy above the bandgap and (b) the resulting carrier distribution of electrons and holes as well as its subsequent energy relaxation due to (c) electron-phonon scattering, (d) electron-electron scattering, and (e) both types of processes (see text). Reprinted from [110]

the carriers may transfer a significant fraction of their initial kinetic energy to the lattice. Since optical phonons in the relevant region close to the center of the Brillouin zone have a negligible dispersion, this leads to the build-up of the so-called phonon-replica of the initial distribution shifted downward by multiples of the phonon energy (see Fig. 2.7c). The scattering among the electrons themselves due to the Coulomb interaction, on the other hand, conserves the total kinetic energy; however it leads to a spreading in \mathbf{k} -space (see Fig. 2.7d) and eventually, at later times, to a Fermi–Dirac distribution where the temperature is determined by the initial excess energy. If, as is always the case in a real semiconductor, both mechanisms are present, both energy relaxation and thermalization toward a Fermi–Dirac distribution occur simultaneously (see Fig. 2.7e), the respective time-scales, however, being strongly dependent on the excitation conditions, in particular on the carrier density.

These thermalization and relaxation processes have been studied in great detail in the past three decades both experimentally and theoretically in bulk semiconductor materials as well as in a variety of nanostructures. The most commonly used experimental techniques for these studies have been luminescence, where the photons created by the radiative recombination of electrons and holes are detected, and pump-probe (PP) measurements, where the change in the absorption (or reflection) of a probe beam caused by the prior excitation of electron–hole pairs by the pump beam is observed. While it is nearly impossible to quote all the work, we just mention some of the phenomena which have turned out to be important under certain excitation conditions. In the case of sufficiently high excitation densities it has been found that the distribution function of LO-phonons is driven substantially out-of-equilibrium and that this so-called hot-phonon effect, described in Sect. 6.3, may drastically reduce the cooling process (see, e.g., [121]). The dynamics of the nonequilibrium phonons has been studied directly by Raman measurements (see, e.g., [122]). If the excitation energy is above the threshold for transitions to satellite valleys in the conduction band, intervalley scattering due to carrier–phonon interaction is a very effective process mainly because of the high density of states in these valleys (see, e.g., [123]).

Starting from the mid-1980s the field of coherent excitations in semiconductors became an increasingly active research area. Even if in the measurements mentioned above essentially carrier relaxation processes are monitored, it turned out that also in these signals features related to coherence are present; in particular, under certain conditions coherent aspects may be dominant. In the case of PP spectra this holds most prominently if the pump pulse is non-resonant with optical transitions, i.e., if it is tuned into the bandgap region where it does not create real populations. Here, it gives rise to shifts and splittings of the exciton line which is known as the optical Stark effect. Starting from the mid-1980s this effect has been extensively investigated (see, e.g., [124]).

Besides PP and luminescence measurements, however, there are other techniques which rely completely on the phase coherence in the carrier system,

thus providing a direct information on the dynamics of coherent interband and intraband polarizations. The most prominent among these techniques are four-wave-mixing (FWM) experiments and the detection of coherently emitted radiation in the terahertz spectral region.

As anticipated, many solid-state systems exhibit an inhomogeneous broadening (see Fig. 2.6). In the case of a semiconductor in the excitonic region this is typically due to some structural disorder in the sample while in the band-to-band continuum region the \mathbf{k} -dependence of transition energies may also be interpreted as such a broadening. Then, as anticipated, the total polarization rapidly decays due to destructive interference of the different frequency components and, thus, it is difficult to extract information on the true loss of phase coherence due to decoherence processes. In the case of magnetic resonance the technique of spin echoes has been introduced already in 1950 by Erwin L. Hahn [125]; the latter is able to eliminate the decay due to inhomogeneous broadening (see (2.48) in Sect. 2.2), and decoherence times – the so-called T_2 times – can be measured. In the 1960s, due to the availability of laser sources, echo experiments have been brought into the optical spectral range; photon echoes have been first observed in ruby [126]. Since in semiconductor materials decoherence is much faster, very short pulses are required here for such techniques. In 1985 photon echoes from delocalized excitons in semiconductors have been observed by using 7 ps laser pulses [127], and a few years later, photon echoes from band-to-band transitions have been measured with 6 fs pulses [128]. These photon echoes are typically studied by means of degenerate FWM measurements which will be described below. With such experiments an excitonic phase-coherence time-scale of about 7 ps and a well precise density dependence have been established.

But such experiments do not only provide information on the decay of carrier phase coherence; instead, many other coherent phenomena have been studied in the past, like quantum beats due to quantum-mechanical superpositions of electronic states (see, e.g., [129–132]). If such superpositions are excited between states with different spatial localizations, they are the source of an electromagnetic radiation with a frequency given by the energy splitting (between these states). This frequency is typically in the terahertz spectral range, and in this regime the electric-field strength may be directly measured, in contrast to the optical regime where typically only intensities can be measured. Such a terahertz emission has first been observed from asymmetric double quantum-well structures [133], thus opening the way to the field of terahertz spectroscopy in semiconductors (see, e.g., [134] and references therein).

Another direct approach to coherent phenomena is the technique of coherent control by two (temporally separated) phase-locked optical pulses (see, e.g., [135]). If the optical polarization created by the first pulse is still present in the sample, this polarization can constructively or destructively interfere with the second pulse, leading to a quantum-mechanical carrier dynamics which strongly depends on the relative phase of the two pulses. Such

non-trivial dynamics can then be probed by the reflection or transmission change via, e.g., PP measurements, or by monitoring the FWM signal induced by a third pulse. It should be noted that there is a second type of coherent-control experiments where a superposition of a one-photon and a two- or three-photon excitation by two simultaneous pulses is used to control the final state in the case of degeneracy (see, e.g., [136] and references therein).

Generally speaking, coherent control makes use of the full time-dependence of the electric-field vector of the light pulse including intensity, phase, and polarization. An overview of different applications of coherent-control techniques can be found in [137].

Coherent phenomena do not only take place in the electronic subsystem of the semiconductor. Indeed, in spatially inhomogeneous systems or in systems with sufficiently low symmetry the optical excitation may also give rise to the generation of coherent phonons, i.e., phonons with a non-vanishing expectation value of the lattice displacement, in contrast to incoherent phonons where only the mean square displacement is non-zero. The excitation of coherent phonons in semiconductors has first been observed by optical excitation in the surface field of n-doped GaAs [138]. Here, the differential reflectivity change exhibited clear modulations with the phonon frequency. If the generated phonons are infrared-active they will also directly emit an electromagnetic radiation with the corresponding frequency in the terahertz range which again can be detected in the way described above.

As mentioned previously, for the study of carrier energy-relaxation processes essentially two different classes of experiments have been employed: luminescence and pump-probe measurements. In both cases a pump pulse is used to generate electron-hole pairs, thus bringing the semiconductor material in a state far from thermal equilibrium. In a luminescence experiment the radiation emitted in a direction different from that of the incident pulse due to recombination processes is analyzed spectrally and/or temporally. This is shown schematically in Fig. 2.8a. Depending on the temporal resolution, different techniques have to be employed: A temporal resolution in the range of 10 ps can be achieved by direct techniques, either by using fast photodiodes or a streak camera which provides spectral and temporal information simultaneously. Higher time resolution is obtained by gating the luminescence signal with a second delayed laser pulse. Both signal and delayed pulse are focused on a nonlinear crystal, which creates a sum-frequency signal only in the presence of such gating pulse. In this upconversion technique the temporal resolution is limited by the laser-pulse duration only; thus, resolutions in the 10 fs range are possible.

In an intrinsic semiconductor the luminescence is due to the recombination of an electron in the conduction band with a hole in the valence band. In a fully incoherent picture, according to Fermi's golden rule, the signal is essentially proportional to the product of the distribution functions of electrons and holes. This complicates the interpretation of experimental results. An alternative approach is the use of doped semiconductors where, e.g., in p-doped samples,

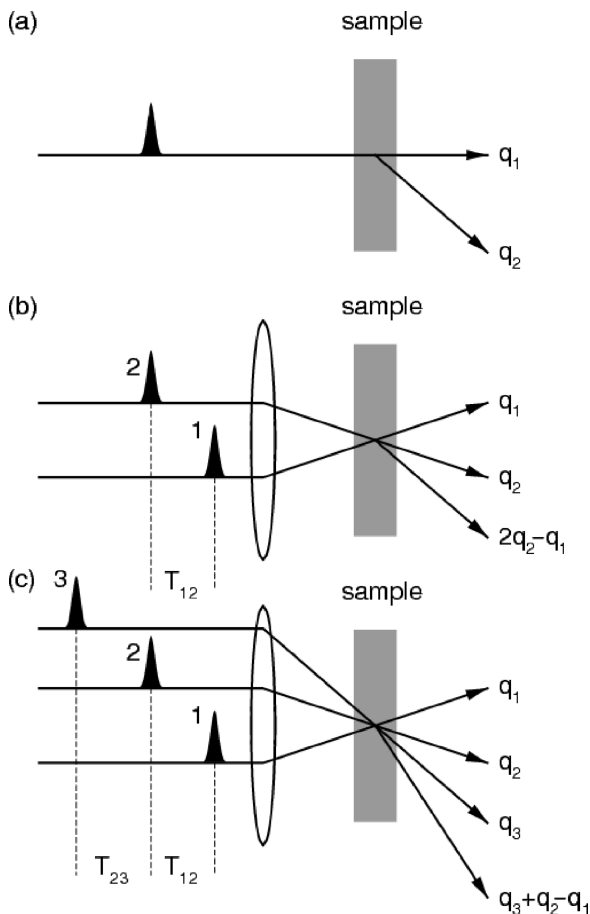


Fig. 2.8. Schematics of typical experimental setups for the study of ultrafast phenomena in semiconductor materials. In (a) the sample is excited by a single pulse and the secondary emission (resonant Rayleigh scattering or luminescence) is detected in a direction different from the incident one; (b) refers to pump-probe experiments or four-wave-mixing in the two-pulse self-diffraction geometry; and (c) refers to general three-pulse four-wave-mixing experiments (see text). Reprinted from [110]

the band-to-acceptor luminescence monitors directly the distribution function of electrons.

In a pump-probe experiment the semiconductor is excited by a pump pulse traveling in a direction q_1 (see pulse 1 in Fig. 2.8b) and the dynamics of the carriers induced by this excitation is studied by looking at some property related to a delayed probe pulse in a direction q_2 . The most commonly used technique is transmission or reflection spectroscopy, where the change in the transmission or reflection of the probe pulse – induced by the pump – is

measured as a function of the time delay between the two pulses.⁵ By using a broadband probe pulse, differential transmission/reflection spectra are therefore obtained. In a purely incoherent free-carrier picture the absorption is changed due to phase-space filling, and these signals provide information on the sum of the electron and hole populations in the optically coupled states. Again, the interpretation of the results is facilitated if the spectra are determined by a single distribution function. This can be achieved by exploiting optical transitions for the probe in a different spectral range, e.g., by pumping heavy and light holes to conduction-band transitions and probing the split-off to conduction-band transition. A variation of the PP technique previously introduced is the electro-optic sampling, where the difference between two polarization components of the transmitted/reflected signal is analyzed; the latter provides information, e.g., on a birefringence induced by the optically excited dynamics. Instead of measuring the change in the transmitted/reflected signal, the change in the Raman-scattering signal generated by the probe pulse can also be measured. By using this technique the dynamics of photoexcited phonons as well as electronic excitations can be investigated.

It is clear that the interpretation of luminescence and PP experiments in terms of a fully incoherent free-carrier picture is valid only under limited conditions. In intrinsic semiconductors at sufficiently low carrier densities, absorption and luminescence spectra in the region close to the bandgap are strongly dominated by excitonic effects (see Fig. 1.21). Even high up in the band, pump-induced changes in the Coulomb enhancement (see Sect. 1.2.2) may significantly influence PP spectra. Furthermore, on time-scales comparable to or shorter than the characteristic decoherence times, the signals may be considerably modified by coherence effects. Therefore, a detailed analysis of luminescence and PP spectra in the ultrafast regime also provides information on coherent phenomena in the semiconductor material under examination.

The most popular technique which provides direct information on the carrier coherence in the semiconductor is four-wave-mixing spectroscopy. It can be performed both in a two-pulse and in a three-pulse configuration, as shown schematically in Fig. 2.8b,c.⁶ For reasons of clarity, let us start with the three-pulse configuration by assuming that the time delay T_{12} between the two laser pulses 1 and 2 with wavevectors \mathbf{q}_1 and \mathbf{q}_2 is equal to 0. In this case these pulses create an interference pattern with wavevector $\pm(\mathbf{q}_2 - \mathbf{q}_1)$ on the sample which translates into a density grating when the light is absorbed. Such density grating results in a refractive index grating which may diffract a third pulse with incident wavevector \mathbf{q}_3 into various diffraction orders $\mathbf{q}_3 + n(\mathbf{q}_2 - \mathbf{q}_1)$, n being an integer number. In FWM measurements the first diffracted order $n = 1$ is measured; in this case, three incident waves interact giving rise to a fourth emitted wave which explains the name of this

⁵ In Fig. 2.8 only the transmission case is plotted.

⁶ Four-wave-mixing experiments can be performed in a reflection geometry as well.

technique. Access to the coherent polarization in the sample is now obtained if the pulses 1 and 2 are temporally separated. In this case there is no more direct interference pattern on the sample. However, as long as the microscopic interband polarization created by pulse 1 is at least partly still present when pulse 2 arrives, the interaction of a pulse with wavevector \mathbf{q}_2 with the interband polarization in the direction \mathbf{q}_1 again results in a transient grating which can diffract pulse 3. Thus, by varying T_{12} information is obtained on the dynamics and life-time of the polarization, i.e., on the decoherence time. It should be noted that a microscopic interband polarization may still be present even if, in the case of a continuous spectrum due to destructive interference of different microscopic components, there is no more macroscopic polarization in the sample (see Fig. 2.6). This is exactly the reason why FWM spectroscopy may discriminate between homogeneous and inhomogeneous broadening.

In the most frequently used two-pulse setup, pulse 2 simultaneously creates the grating and is diffracted by this grating; therefore it is also called the “self-diffraction geometry.” Besides analyzing the signal in a time-integrated way it can also be spectrally dispersed in a monochromator or temporally resolved by means of an upconversion technique as discussed previously in the case of luminescence, which provides additional information on the dynamics of the interband polarization.

Both PP and FWM experiments can be employed to study coherent-control phenomena. In this case the pulse 1 is replaced by a pair of phase-locked pulses with variable delay traveling in the same direction \mathbf{q}_1 . The carrier dynamics induced by these pulses then depends on the relative phase between these two pulses, and it can be analyzed by the second pulse traveling along the direction \mathbf{q}_2 . Measuring the transmitted signal along \mathbf{q}_2 (or the corresponding reflected direction) and the FWM signal along $2\mathbf{q}_2 - \mathbf{q}_1$ yields in general complementary information on the dynamics of carrier distribution functions and polarizations.

If the optically excited interband polarizations couple electronic states with different spatial localizations, the dynamics is associated with a time-dependent dipole moment which, according to classical electrodynamics, acts as a source of electromagnetic radiation. Often this radiation is in the terahertz spectral range. Indeed, in a typical terahertz-emission experiment a short laser pulse excites the system in a superposition of states, thus creating an intraband polarization; The latter oscillates according to the energy splitting of the corresponding states and emits a pulse of electromagnetic radiation with the respective frequency. This radiation is then collimated and transmitted to an optically gated photoconductive antenna which measures the electric field of the radiation. Thus, the general setup is again according to Fig. 2.8a; the emitted signal in direction \mathbf{q}_2 , however, being in the terahertz spectral region.

For a more detailed discussion of the experimental techniques previously recalled, we refer the reader to the book by Jagdeep Shah [90].

2.6 The Wide Family of Quantum Devices

The wide family of the so-called quantum devices [51, 56–69] can be divided into two main classes: a first one grouping semiconductor devices characterized by a genuine quantum-mechanical behavior of their electronic subsystem and a second one which comprises low-dimensional nanostructures whose optoelectronic response in steady-state conditions may be safely treated within the semiclassical picture previously introduced.

Devices within the first class – characterized by a relatively weak coupling of the electronic subsystem to the host material – are natural candidates for the implementation of quantum-information/computation processing [139–152]. These include, in particular, semiconductor quantum-dot structures [42, 44–49], for which all-optical implementations have been recently proposed (see, e.g., [51, 69] and references therein). In this case, the pure quantum-mechanical carrier dynamics is only weakly disturbed by dissipation and decoherence processes; therefore, the latter are usually described in terms of relatively simplified models.

Conversely, quantum devices in the second class – in spite of their partially discrete energy spectrum due to spatial quantum confinement – exhibit a carrier dynamics which for normal operation conditions can still be described via a semiclassical scattering picture. Such optoelectronic nanostructured devices include multiple-quantum-well and superlattice structures, like quantum-well infrared photodetectors (see, e.g., [64] and references therein) and quantum-cascade lasers (see, e.g., [66] and references therein). These systems are characterized by a strong interplay between coherent dynamics and energy-relaxation/decoherence processes; it follows that for a quantitative description of such non-trivial coherence/dissipation coupling the latter needs to be treated via fully microscopic models (see, e.g., [110]).

Based on the above subdivision, it is quite natural to identify two distinct regimes, determined both by the peculiar features of the nanomaterial involved and by the particular operation conditions. More specifically, as schematically summarized in Fig. 2.9, we deal with two different regimes, the semiclassical and the quantum-mechanical one. For both regimes it is possible to adopt a phenomenological description or a microscopic treatment of the problem. In particular, according to the classification scheme of Fig. 2.9, semiconductor devices operating within the semiclassical regime may be described either phenomenologically via simplified rate-equation models or microscopically via

	Semiclassical Regime	Quantum-mechanical Regime
Phenomenological Treatments	<i>Simplified Rate-Equation Models</i>	<i>Simplified Bloch-Equation Models</i>
Microscopic Treatments	<i>Realistic Boltzmann-like Approaches</i>	<i>Realistic Density-Matrix Approaches</i>

Fig. 2.9. General classification scheme of the various approaches employed for the study of semiconductor quantum devices (see text)

realistic Boltzmann-like treatments, while for devices operating within the quantum-mechanical regime we may adopt either a phenomenological description based on simplified Bloch-equation models or a microscopic description based, e.g., on realistic density-matrix or Green's function treatments (see Chap. 3).

A common feature of all phenomenological treatments is the description of electron-electron as well as electron-environment interaction mechanisms via relaxation-time models (see, e.g., (1.76), (2.40), and (2.43)); conversely, all microscopic treatments are based on a detailed knowledge of the various interaction Hamiltonians, and therefore they do not require any phenomenological parameter.

As anticipated, the primary goal of this book is to provide a cohesive description of many diverse quantum nanodevices, via a unified and fully microscopic density-matrix treatment of coherent versus incoherent electro-optical processes in semiconductor nanostructures.

Theory of Semiconductor Quantum Devices
Microscopic Modeling and Simulation Strategies

Rossi, F.

2011, XIV, 382 p., Hardcover

ISBN: 978-3-642-10555-5